(Received 15 September 2025, Accepted 15 November 2025, Scheduled 2 December 2025)

Design and Analysis of a Six-Phase Hybrid-Excited Reverse-Salient Fault-Tolerant Permanent Magnet Motor for Electric Vehicles

Canwei Zhang, Zhangqi Liu*, Xiping Liu, and Ruipan Lu

School of Electrical Engineering and Automation, Jiangxi University of Science and Technology, Ganzhou 341000, Jiangxi, China

ABSTRACT: Conventional permanent magnet synchronous motors (PMSMs) suffer from limitations in speed regulation range, poor fault tolerance, and restricted torque output in electric vehicle drive applications. To address these limitations, this paper proposes a six-phase, 12-slot/10-pole hybrid-excited reverse-salient fault-tolerant motor (FT-HE-RSPM). To achieve reverse-salient characteristics and regulate the air-gap magnetic field, the rotor adopts segmented permanent magnets and a q-axis magnetic barrier. This design increases the d-axis inductance while reducing the q-axis inductance, achieving the reverse-salient characteristic $L_d > L_q$ under rated conditions. Additionally, both the stator and rotor adopt segmented structures, forming axial magnetic paths via magnetic bridges. The excitation windings are embedded in the stator using non-magnetic materials, and the air-gap magnetic field is regulated by controlling the excitation current. The motor's magnetic field regulation mechanism was analyzed using the equivalent magnetic circuit method. Combined with three-dimensional finite element analysis (3D-FEA), the motor's electromagnetic performance and fault-tolerant characteristics were investigated, leading to the design of a current reconstruction fault-tolerant control strategy for single-phase open-circuit faults. Results demonstrate that this motor exhibits high torque output capability, excellent flux regulation characteristics, high efficiency, and outstanding fault tolerance, meeting the demands of complex operating conditions in electric vehicles.

1. INTRODUCTION

In recent years, energy shortages and environmental pollution have intensified globally. The pursuit of "carbon peak" and "carbon neutrality" has propelled electric vehicles (EVs) into the spotlight, attracting significant research and development interest [1, 2]. The electric motor, as the core drive component, is a critical determinant of the vehicle's overall efficiency and reliability. Permanent magnet synchronous motors (PMSMs) are extensively used in electric vehicle drive systems due to their high efficiency and power density [3]. However, the intrinsic high coercivity of permanent magnets complicates the regulation of the air-gap magnetic flux, which constrains the flux-weakening capability and, consequently, the maximum operating speed. To extend this speed range, several solutions have been explored, including hybrid excitation motors, permanent magnet memory motors, and reverse-salient motors [4, 5]. Among them, hybrid excitation permanent magnet motor (HE-PMM), which synergizes the advantages of permanent magnet and electrically excited machines, has received considerable attention. Based on the location of the field winding, HE-PMMs can be classified into three categories: those with the winding placed on the rotor, the stator, or at the motor's end.

Ref. [6] presents an end-mounted field winding design. This winding generates an axial magnetic field through a magnetic bridge to modulate the main air-gap flux. Refs. [7, 8] propose a topology where the field winding (FW) is placed on the rotor. Results demonstrate that the FW assistance significantly enhances both the flux-weakening capability and output torque. However, this rotor-mounted FW configuration necessitates brushes and slip rings, which compromises system reliability and increases maintenance requirements. To eliminate brushes and slip rings in hybrid excitation motors (HEMs), the design in [9] fixes the field winding to the end cover. Brushless excitation is achieved by utilizing an auxiliary air-gap between the rotor core and magnetic bridge. Refs. [10–13] locate the field winding on the stator. For instance, [11] proposes a brushless topology that employs extended magnetic bridges embedded with field windings; [12] arranges permanent magnets on both the stator teeth and yoke to generate a parallel dual-permanent-magnet flux path for torque enhancement. This is complemented by field windings that produce a DC flux for flux-weakening control. Ref. [13] proposes a novel brushless excitation scheme where a 3rd harmonic stator magnetomotive force (MMF), generated by injecting a zero-sequence current, is used to induce voltage in a rotor harmonic winding for rectification and field excitation. However, this configuration, in which both the field and armature windings are located on the stator, can lead to an increase in stator volume and complexity.

Reverse-salient permanent magnet motors (RSPMs) are widely used in electric vehicles owing to their advantageous characteristics: a wide constant-power speed range, low weak-magnetization current i_d, and reduced risk of irreversible demagnetization. Conventional permanent magnet synchronous motors (PMSMs) typically exhibit obverse-salient

* Corresponding author: Zhangqi Liu (liuzhq@jxust.edu.cn).

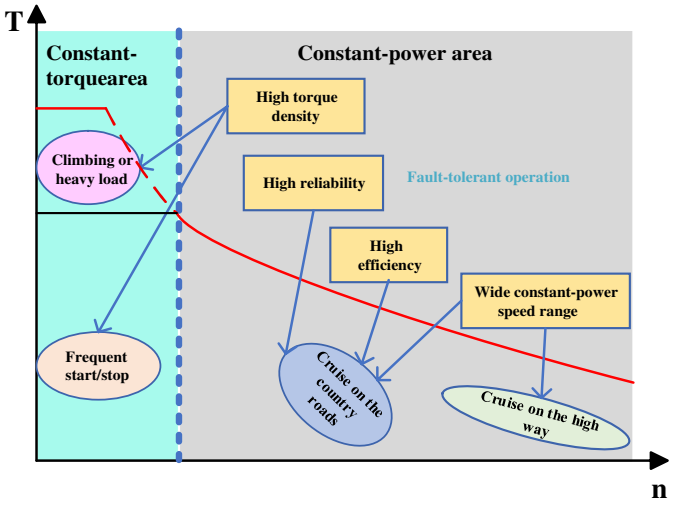

FIGURE 1. Complex conditions of the motor drive system.

(OS) characteristics, where $L_d < L_q$. In contrast, RSPMs are characterized by $L_d > L_q$ [14, 15]. To achieve this reverse-salient characteristic, numerous studies have been conducted, leading to various proposed topological structures. Refs. [16, 17] effectively widen the speed range and achieve reverse-salient characteristic by employing q-axis flux barriers, segmented permanent magnets, and non-uniform air-gaps. Ref. [18] designs two prototypes. In one, a magnetic bridge is introduced into the d-axis magnetic circuit; its low reluctance is leveraged to decrease the total d-axis reluctance. In the other, an arc-shaped flux barrier is installed on the q-axis to minimize the q-axis inductance. This approach successfully realizes the reverse-salient characteristic.

However, the majority of automotive drive motors still utilize conventional three-phase windings. These systems exhibit low reliability under fault conditions, such as open-circuit or short-circuit faults. The drive systems of electric vehicles must demonstrate high operational reliability to ensure vehicle safety. Therefore, enhancing both the wide-speed operational capability and fault-tolerant capability of motors is critically important.

Refs. [19–21] propose various multi-phase hybrid excitation motor topologies, all featuring a single-layer winding structure. This single-layer design provides enhanced phase-to-phase isolation, and the field windings can operate in a brushless mode. Refs. [22, 23] propose five-phase reverse-salient motors that balance reverse-salient characteristics and fault tolerance through increased phase number, q-axis flux barriers, and optimized rotor design. However, simultaneously optimizing both fault tolerance and reverse-salient characteristics presents significant challenges. Fault-tolerant motors require specific slot-pole combinations, typically where the difference between slot and pole numbers is 2 [24]. This configuration often exhibits multi-pole characteristics, which limits the available space for incorporating flux barriers in the rotor. Achieving reverse-salient characteristics typically requires adding flux barriers along the q-axis to increase q-axis magnetic reluctance, creating a structural conflict with the requirements for fault-tolerant performance.

To address the challenges associated with air-gap flux regulation in conventional motors and the conflicting design requirements between reverse-salient characteristics and fault tolerance, this paper proposes a hybrid-excited reverse-salient fault-tolerant motor. Reverse-salient characteristics are achieved through a q-axis flux barrier and segmented permanent magnets. An excitation winding is incorporated, enabling brushless operation via a segmented rotor-stator structure and an integrated magnetic bridge. The motor's performance was validated through equivalent magnetic circuit analysis and 3D finite element analysis, demonstrating excellent flux-weakening capability and strong fault-tolerant performance.

2. EVS WORKING CONDITION ANALYSIS AND DESIGN REQUIREMENTS

2.1. EVS Working Condition Analysis

Electric vehicles operate under diverse and complex conditions, frequently traversing urban, rural, and mountainous terrain. The motor operates under various conditions including frequent start-stop cycles, acceleration and deceleration, heavy-load hill climbing, and high-speed cruising. As shown in Figure 1, Urban Dynamometer Driving Schedule (UDDS) is widely used to simulate and evaluate urban and suburban driving conditions. The UDDS encompasses four distinct operating modes: Mode I (Low speed/heavy load): Requires high torque output and strong load-bearing capacity. Mode II (Low speed/light load): Demands high output torque and operational efficiency. For frequent start-stop operations caused by traffic signals and congestion, high motor efficiency is essential to minimizing energy losses. Mode III (High speed/heavy load): Vehicles operate near the motor's rated speed. Mode IV (High speed/light load): Requires operation in a constant-power speed range 3–5 times of the rated speed, necessitating an extended speed regulation range. Speed distribution analysis shows 35% operation in low-speed zones and 65% in high-speed zones. Load requirements primarily involve two scenarios: low-speed heavy-load and high-speed light-load operation. Low-speed heavy-load conditions demand high torque and efficiency, while high-speed light-load conditions require wide speed regulation range, high output power, and adequate torque. Beyond efficiency, motor reliability must be ensured. Potential failure modes include winding open-circuits and short-circuits. The drive motor must possess robust fault-tolerant capabilities to ensure operational reliability and safety under fault conditions.

2.2. Design Requirements Analysis for EV

Developing motors and drive systems that combine high power density, wide speed regulation range, and excellent fault tolerance is crucial for enhancing electric vehicle performance and promoting their widespread adoption.

For permanent magnet motors, the terminal voltage u and electromagnetic torque T_{em} are expressed as:

$$u = \omega\sqrt{(L_q i_q)^2 + (L_d i_d + \psi_{PM})^2} \tag{1}$$

$$T_{\text{em}} = \frac{m}{2} p \left[\psi_{PM} i_q + (L_d - L_q)\, i_d i_q\right] \tag{2}$$

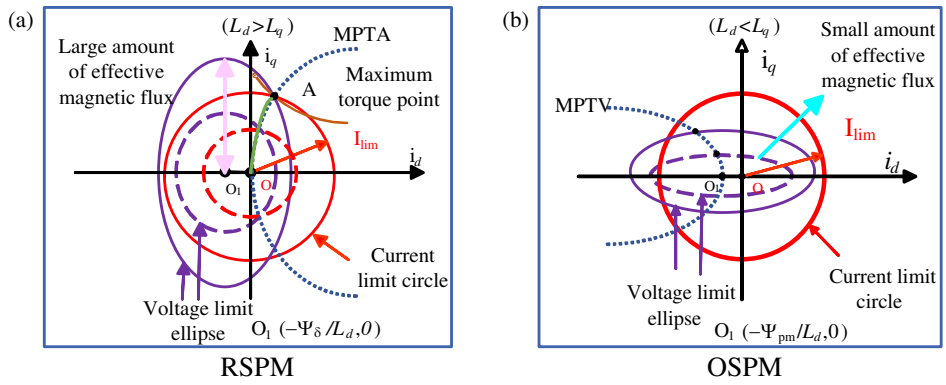

FIGURE 2. Current vector trajectory circle.

where ω denotes the mechanical angular velocity; L_q and L_d are the q-axis and d-axis inductances, respectively; i_q and i_d are the q-axis and d-axis currents, respectively; ψ_{PM} is the permanent magnet flux linkage; m is the number of phases; p is the number of pole pairs.

Figure 2 illustrates the current vector trajectories of a conventional obverse-salient permanent magnet motors (OSPMs) and reverse-salient permanent magnet motors (RSPMs) under the maximum torque per ampere (MTPA) control strategy. As shown, the RSPM exhibits an additional flux-intensifying (FI) operating region where the d-axis current i_d is positive. This results from its reverse-salient characteristic where the d-axis inductance L_d exceeds the q-axis inductance L_q. Furthermore, according to the derivations of Equations (1) and (2), under constant current amplitude conditions, a larger L_d results in a wider speed regulation range. In contrast, OSPM motors can only produce positive reluctance torque when i_d is negative. This operational requirement increases the risk of irreversible demagnetization of the permanent magnets. It is worth noticing that the reluctance torque of RSPMs increases with the inductance difference (L_d-L_q). This demonstrates that pronounced reverse-salient characteristics significantly enhance the motor's torque output capability.

Hybrid excitation motors (HEMs) synergize the advantages of permanent magnet motors and electrically excited motors, enabling effective regulation of the air-gap magnetic flux through control of the field winding current. Neglecting magnetic coupling effects, the voltage equation for the auxiliary field winding and the additional torque component can be expressed as:

$$u_f = R_f I_f + \frac{\mathrm{d}\psi_f}{\mathrm{d}t} \tag{3}$$

$$T_f = \frac{m}{2} p\, L_{sf} I_f\, (i_q - i_d) \tag{4}$$

where R_f is the resistance of the field winding, I_f the applied field winding current, ψ_f the flux linkage generated by the field winding, and L_{sf} the mutual inductance between the field winding and armature winding. The analysis of Equations (3) and (4) reveals that HEMs achieve dual control capabilities through flexible adjustment of the field winding current's magnitude and direction: Firstly, it enables flux-weakening control, significantly expanding the motor's constant-power speed range. Secondly, it provides flux-strengthening capability, effectively meeting the automotive requirement for high torque output at low speeds.

Winding faults during motor operation are primarily categorized as open-circuit or short-circuit faults. To mitigate open-circuit faults, fault-tolerant motors employ additional winding channels or phases. This design enhances operational reliability over conventional three-phase motors by allowing continued operation even after isolating a faulty phase. For short-circuit faults, the short-circuit current suppression capability is a key metric for evaluating motor fault tolerance. In Figure 3, E_0 represents the no-load back electromotive force (back-EMF), while X_d and X_q are the d-axis and q-axis reactance, respectively. I_d is the d-axis current. It can be observed that under the same terminal voltage U, RSPM exhibits a lower no-load back EMF than OSPM motor. Short-circuit characteristic analysis indicates that a lower no-load back Electromotive Force (EMF) results in reduced peak and steady-state short-circuit currents, thereby providing the RSPM with superior short-circuit current suppression capability.

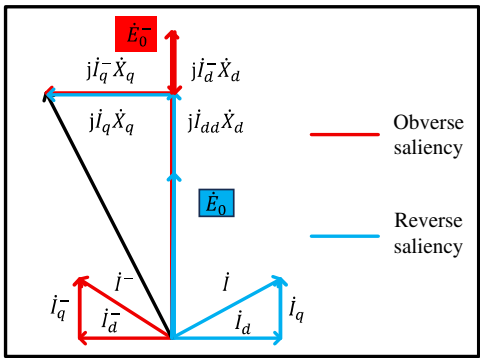

FIGURE 3. Phasor diagram of motor.

The above analysis demonstrates that motors featuring hybrid excitation and reverse-salient characteristics can enhance motor torque, regulate air-gap magnetic field, and expand motor speed regulation range. Integrating these characteristics, a novel six-phase hybrid excitation reverse-salient fault-tolerant motor (FT-HE-RSPM) is proposed.

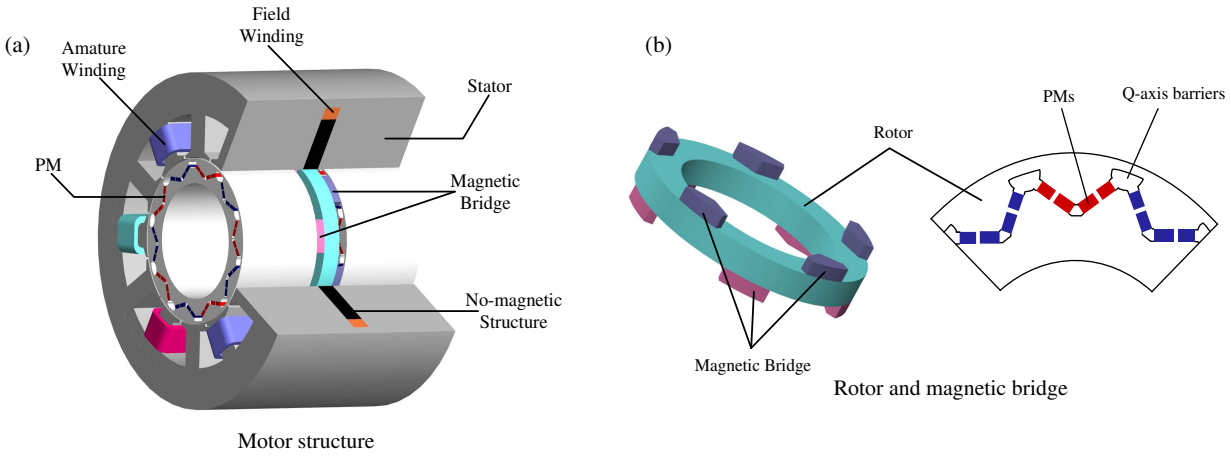

FIGURE 4. Motor topology.

3. TOPOLOGY OF THE MOTOR AND MAGNETIC CIRCUIT

3.1. Topology of Motor

The topology of the proposed FT-HE-RSPM is illustrated in Figure 4. The motor comprises several core components: stator, rotor, segmented permanent magnets, armature winding, field winding, stator rear yoke, and magnetic bridge.

To achieve reverse-salient characteristics, the rotor-mounted permanent magnets are segmented into two segments, and a q-axis magnetic barrier is incorporated to effectively increase the q-axis magnetic reluctance and reduce the q-axis inductance.

The stator employs a single-layer fractional-slot concentrated winding configuration. This winding configuration offers several advantages: short end-turn length, reduced copper losses, high efficiency, high slot fill factor, and minimal cogging torque. Furthermore, in this single-layer concentrated winding arrangement, the stator teeth without windings function as fault-tolerant teeth, providing physical isolation that ensures decoupled electrical circuits, magnetic paths, and thermal fields between phases. This effectively reduces mutual magnetic, electrical, and thermal coupling, thereby enhancing the fault tolerance capability. However, fractional-slot concentrated windings introduce higher-order harmonics into the back EMF and magnetomotive force, which may increase torque ripple and eddy-current losses [25].

In the magnetic circuit design, the stator core adopts a three-segment structure: silicon steel laminations on both sides with an aluminum oxide (Al_2O_3) alloy layer in the middle. The field winding is wound around a non-magnetic material and housed within the rear yoke. Similarly, the rotor core is divided into three segments. The two outer segments feature a conventional spoke-type permanent magnet arrangement. The middle segment contains no permanent magnets. The two outer segmented rotors are connected to the middle rotor via magnetic bridges, forming an axial magnetic circuit. The magnetic bridge is specifically designed to provide a low-reluctance axial path for the magnetic flux generated by the field winding. This configuration significantly simplifies the excitation system arrangement while enabling fully enclosed, brushless operation without slip rings.

3.2. Magnetic Field Regulation Mechanism

When operating under permanent magnet excitation only, the FT-HE-RSPM operates on the same principle as a conventional permanent magnet motor. As shown in Figure 5, the magnetic field regulation mechanism can be analyzed using the d-axis equivalent magnetic circuit. Neglecting the axial reluctance of the solid iron core, the air-gap flux Φ_δ can be expressed by Equation (5). In Equation (6), ξ represents the flux shunting factor, which quantifies the proportion of permanent magnet flux that is bypassed through the magnetic bridge. A value of $\xi < 1$ indicates effective flux regulation capability and a reduction in the effective PM reluctance, thereby facilitating the reverse-salient characteristic. The air-gap flux Φ_δ is influenced by both the magnetomotive force (MMF) and magnetic reluctance.

$$\Phi_\delta = \frac{F_{ad} + F_w + 2\xi F_{PM}}{2R_\delta + R_s + R_r + 2\xi R_{PM}} \tag{5}$$

$$\xi = \frac{R_\sigma\left(i_d, i_q\right)}{R_{PM} + R_\sigma\left(i_d, i_q\right)} \tag{6}$$

where F_{PM} is the PM MMF, F_{ad} is the d-axis armature winding MMF, F_w the MMF produced by the field winding, R_s the stator core reluctance, R_r the rotor core reluctance, R_δ the air-gap reluctance, R_{pm} the PM reluctance, and $R_\sigma(i_d, i_q)$ the magnetic bridge reluctance.

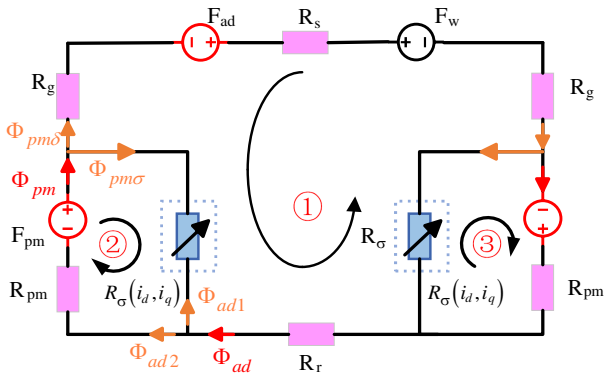

FIGURE 5. D-axis equivalent magnetic circuit.

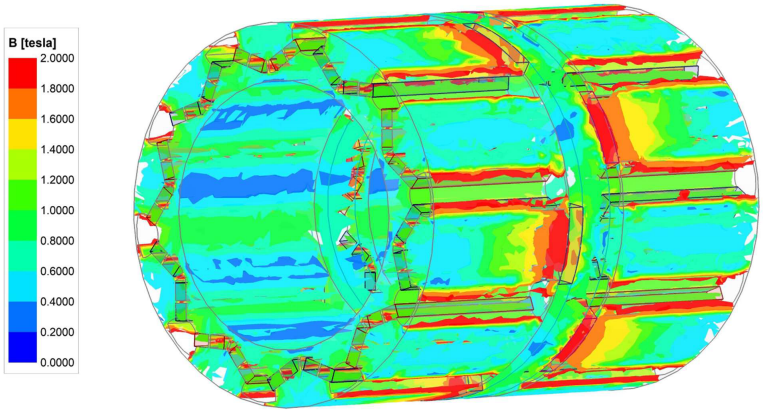

FIGURE 6. Flux density distribution.

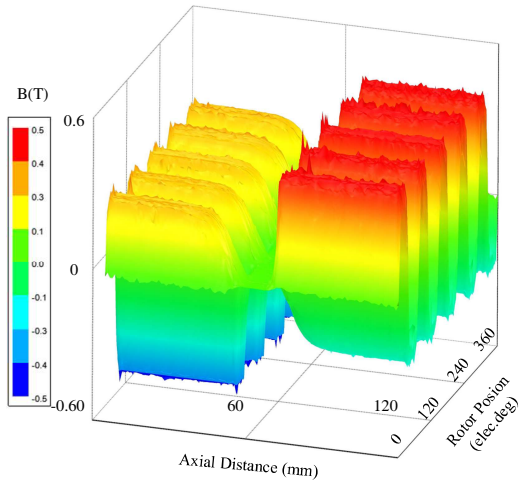

FIGURE 7. Air-gap flux density.

Since the magnetic bridge reluctance $R_\sigma(i_d, i_q)$ is in parallel with the PM reluctance R_{PM}, Equation (6) shows that ξ is always less than 1. This significantly reduces the difficulty of regulating the PM magnetic field. Furthermore, the equivalent reluctance of this parallel combination is lower than R_{PM} alone, which directly increases the d-axis inductance L_d and consequently extends the motor's constant-power speed range.

The total permanent magnet flux Φ_{PM} splits into two components: the main PM flux $\Phi_{PM\delta}$, which links the armature winding, and the PM leakage flux $\Phi_{PM\sigma}$ which forms a closed loop through the magnetic bridge reluctance $R_\sigma(i_d, i_q)$ as shown in Loops 2 and 3 of Figure 5. The flux produced by the armature MMF F_{ad} also passes through the magnetic bridge, as indicated by Loop 1. The magnitude of F_{ad} influences the saturation level of the magnetic bridge, thereby varying its reluctance $R_\sigma(i_d, i_q)$.

When i_d is a flux-strengthening current, F_{ad} and F_{PM} are oriented in the same direction. However, in Loops 2 and 3, the flux component Φ_{ad1} produced by F_{ad} opposes the main PM flux $\Phi_{PM\delta}$. Consequently, under a flux-strengthening i_d, the PM leakage flux $\Phi_{PM\sigma}$ increases, while the main PM flux $\Phi_{PM\delta}$ decreases accordingly. This process demonstrates the armature current's regulatory mechanism on the main PM flux.

When the motor flux is generated by both the PMs and the field winding, the MMF produced by the field winding F_w can be considered as linearly superimposed on the magnetic circuit. When I_f is a flux-strengthening current, F_w and F_{PM} are co-directional, enhancing the air-gap flux. Conversely, when I_f is a flux-weakening current, F_w and F_{PM} are oppositely directed, reducing the air-gap flux. By adjusting the magnitude and direction of the field winding current I_f, the main air-gap flux can be effectively regulated. This process illustrates the control mechanism of the field winding current over the air-gap magnetic field.

4. ELECTROMAGNETIC PERFORMANCE ANALYSIS

To validate the effectiveness of the proposed motor, its electromagnetic characteristics and fault-tolerant performance were analyzed using the three-dimensional finite element method (3D FEM) conducted with ANSYS Maxwell. The key design parameters and geometric dimensions of the motor are summarized in Table 1.

TABLE 1. Harmonic analysis of the back-EMFs.

Items	FT-HE-RSPM
Rated output power (kW)	2
Phase number	6
Rated Current (A)	15
Rated voltage (V)	125
Air-gap length (mm)	0.7
Rated speed (rpm)	1500
PM material	N42SH
Stator and rotor core materials	DW310_35
Out diameter of the stator (mm)	150
Out diameter of the rotor (mm)	87
Slots/Poles	12/10
PM width (mm)	3
Armature winding turns	40
Field winding turns	20
Axial Length (mm)	120

4.1. Flux Density Distribution, Air-Gap Flux Density and Leakage Flux Characteristics

When the FT-HE-RSPM is excited solely by the permanent magnets, the magnetic flux is generated entirely through the permanent magnet synchronous motor principle. The magnetic flux density distribution under no-load condition and PM excitation only ($I_f = 0$ A) at rated speed is shown in Figure 6. The cross-section shows the central plane of the motor. The region of the central magnetic bridge is highlighted, showing a flux density of 1.46 T and forming an internal axial flux path. When the motor operates in hybrid excitation mode, the magnetic flux generated by the field winding current can pass through the ax-

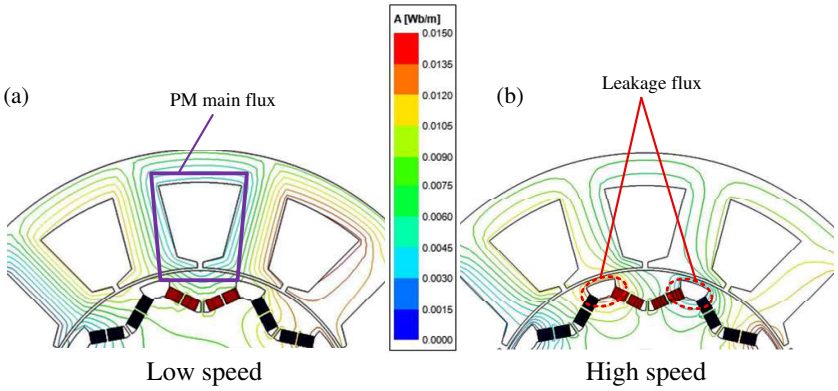

FIGURE 8. Magnetic lines of flux.

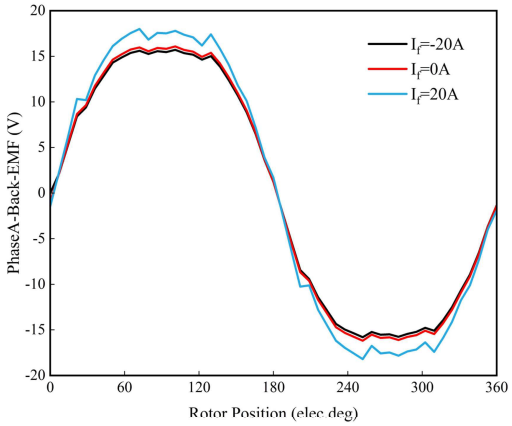

FIGURE 9. No-load-back-EMF.

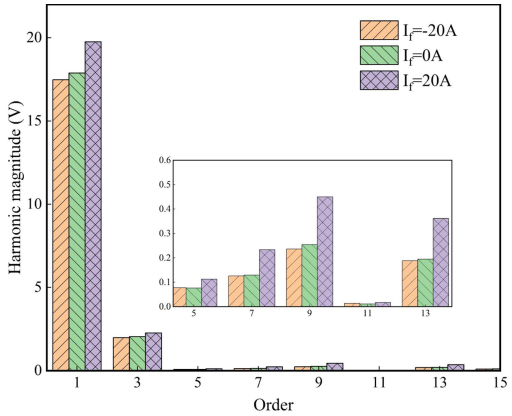

FIGURE 10. Harmonic analysis of the back-EMFs.

ial magnetic circuit. It is noteworthy that the magnetic bridge and its adjacent components exhibit relatively high flux density, which is an inherent feature of the proposed topology. The magnetic field generated by the field winding forms an axial internal circuit through the bridge and the segmented rotor. By applying a field current of appropriate magnitude and polarity under different operating conditions, the permanent magnet flux can be effectively weakened or strengthened, thereby enabling controlled saturation levels in these critical regions and ensuring reliable performance under demanding conditions.

The air-gap flux can thus be regulated by controlling the magnitude and direction of the field winding current. Figure 7 shows the air-gap flux density waveform. It should be noted that due to the segmented structure of the motor in the axial direction, the air-gap magnetic field may exhibit a nonuniform distribution along the entire axial length. As a result, it is impractical to quantify the sinusoidal quality of the air-gap field using a single two-dimensional curve. Nevertheless, qualitative three-dimensional analysis confirms that the air-gap field maintains a satisfactory sinusoidal waveform.

The design of a q-axis magnetic barrier and segmented permanent magnets in the rotor inevitably leads to localized flux leakage around these features during operation. Figure 8 shows the magnetic flux line distribution under low-speed and high-speed operating conditions. During low-speed operation, the effective flux linkage is maintained between 0.008 Wb and 0.012 Wb with minimal leakage paths. Most of the flux generated by the PMs passes through the air-gap, which meets the requirement for high-torque output at low speeds. Conversely, during high-speed operation, significant flux leakage occurs near the magnetic barriers, restricting the effective flux linkage to a range of 0.004 Wb to 0.007 Wb. This intentionally enhanced flux leakage at high speeds reduces the overall air-gap flux density, thereby lowering core losses and facilitating efficient flux-weakening operation for an extended constant-power speed range.

4.2. No-Load Back EMF

Figure 9 shows that under the rated speed of 1500 r/min, the no-load back EMF of the proposed motor reaches 16.08 V with a total harmonic distortion (THD) of 11.5%. The fast Fourier transform (FFT) analysis in Figure 10 confirms its sinusoidal quality. The analysis further verifies the favorable sinusoidal distribution of the air-gap flux. Meanwhile, the high quality of the air-gap field and the resulting back-EMF waveform is a key factor in achieving low torque ripple, as it minimizes the harmonic content that contributes to output torque. Despite some harmonic distortion from the fractional-slot concentrated winding, the optimized q-axis magnetic barrier maintains satisfactory waveform characteristics.

With a field winding current of $I_f = 20$ A, the back EMF increases to 18.01 V (THD = 11.9%), representing a 12.5%

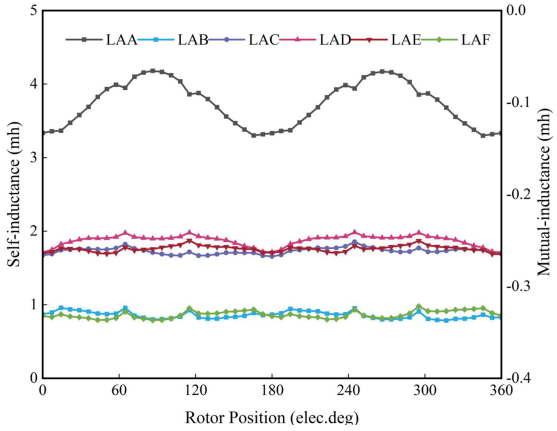

FIGURE 11. No-load inductances characteristics.

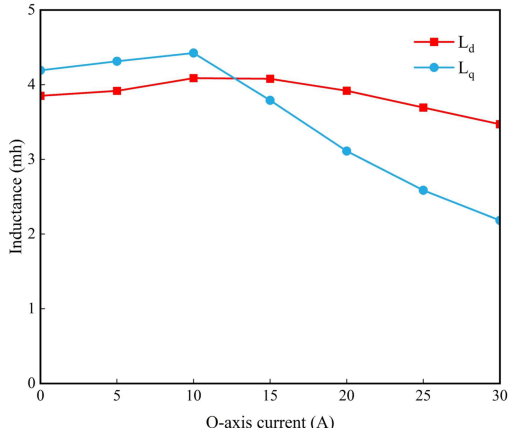

FIGURE 12. d-and q-axis inductance characteristics.

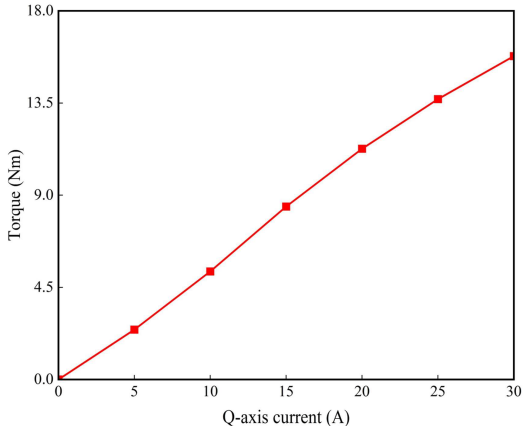

FIGURE 13. Torque versus q-axis current.

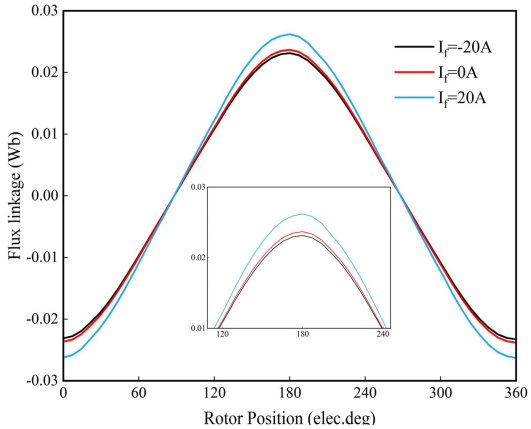

FIGURE 14. Waveforms of Flux linkage.

enhancement compared to PM-only excitation. Conversely, at $I_f = -20$ A, it decreases to 15.7 V (THD = 11.6%). These results validate the effective flux-regulation capability of the hybrid excitation design.

4.3. Inductance Characteristics

Inductance, as one of the important characteristics of electric motors, has profound and multifaceted influences on motor performance, operation, and control. Figure 11 shows Phase A inductance characteristics of the FT-HE-RSPM under no-load conditions. The self-inductance is 3.63 mH; the mutual inductance between adjacent phases is approximately 0.27 mH; and the mutual inductance between non-adjacent phases is about 0.0024 mH. The ratio of mutual inductance to self-inductance is only 7.1%. The ratio of mutual inductance to self-inductance can serve as an indicator of the motor's fault-tolerant capability. A smaller ratio indicates weaker magnetic coupling between phase windings. When a fault occurs in one phase, the interference from the fault current to other healthy phases through mutual inductance is reduced, resulting in superior fault-tolerant performance. This validates the motor's strong fault-tolerant performance. Additionally, the relatively high self-inductance design helps to limit the short-circuit current.

Figure 12 shows the characteristics of the d-axis inductance L_d and q-axis inductance L_q under different q-axis currents. It can be observed that under no-load conditions $L_d < L_q$, as the q-axis current I_q increases, the armature reaction effect and magnetic circuit saturation degree gradually intensify. At $I_q = 13.2$ A, L_d becomes equal to L_q. As I_q continues to increase, $L_d > L_q$. Under the rated condition of $I_q = 15$ A, the reverse-salient ratio L_d/L_q reaches 1.08, and it continues to increase with further the increase in I_q. This phenomenon is attributed to the design of the q-axis magnetic barrier. As I_q increases, the q-axis magnetic reluctance increases, causing the q-axis inductance L_q to decrease at a faster rate. Meanwhile, the segmented permanent magnets allow some magnetic flux lines to bypass the PMs and pass directly through the ferromagnetic material. This results in a longer flux path in the main magnetic circuit and a lower reluctance of the main magnetic circuit, thereby leading to a larger d-axis inductance L_d.

Figure 13 further shows that the motor's torque-current characteristic, and it is important to note that the electromagnetic torque, governed by Equation (2), increases monotonically with I_q throughout this transition. This is because the PM torque component remains the dominant source of torque. The reluctance torque component shifts from being slightly negative to positive, contributing to the overall torque output in the rated operating region without causing a torque drop.

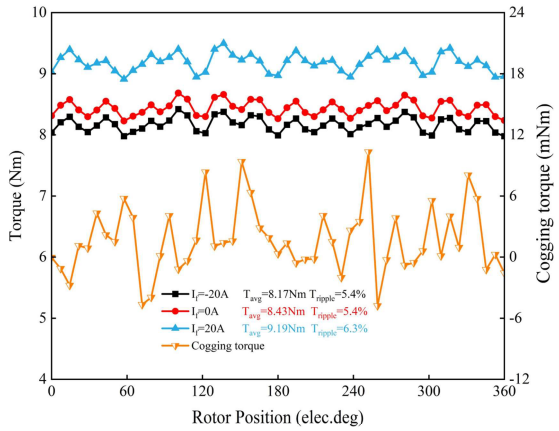

FIGURE 15. Waveforms of output torque.

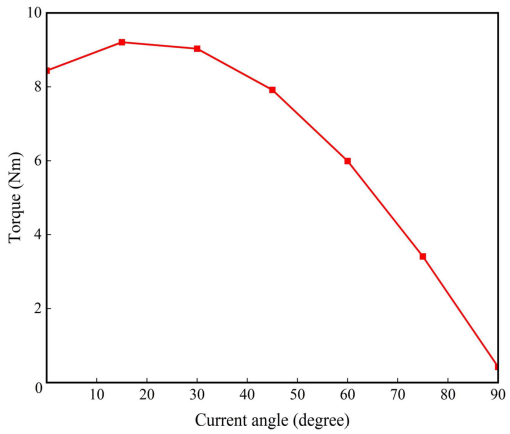

FIGURE 16. Average torque against current angle.

4.4. Flux Linkage

Figure 14 depicts the flux linkage characteristics of phase A winding under different field winding currents. Under the no-load condition (PM excitation only), the maximum flux linkage of phase A is 0.0237 Wb. When $I_f = 20$ A the maximum flux linkage increases to 0.0262 Wb. Conversely, when $I_f = -20$ A, it decreases to 0.0230 Wb.

To quantitatively evaluate the magnetic field regulation capability, a flux regulation factor k_{fr} is introduced [26], which is defined by Equation (7):

$$k_{fr} = \frac{\psi_{HE} - \psi_{PM}}{\psi_{HE}} \times 100\% \tag{7}$$

where ψ_{PM} and ψ_{HE} are the flux linkages produced by the permanent magnets (PMs) and hybrid excitation (HE) system, respectively. The calculation results indicate that the motor exhibits a considerable flux-strengthening capability up to 10.6%, demonstrating its excellent magnetic field regulation performance.

4.5. Torque Characteristics

The electromagnetic torque T_{em} of the FT-HE-RSPM comprises three components: reluctance torque T_{rel}, permanent magnet torque T_{PM}, and an additional torque T_f generated by the field winding. The expressions for each torque component are as follows:

$$T_{rel} = 3pi_d i_q \left(L_d - L_q\right) \tag{8}$$

$$T_f = 3pM_{sf} i_f i_q \tag{9}$$

$$T_{PM} = 3pi_q \psi_{PM} \tag{10}$$

$$T_{em} = T_{PM} + T_{rel} + T_f \tag{11}$$

Compared to conventional motors, the proposed FT-HE-RSPM combines the advantages of both reverse-salient characteristics and hybrid excitation flux regulation capability. On one hand, the reverse-salient characteristic enables a reluctance torque enhancement region even when $i_d > 0$. On the other hand, by controlling the magnitude and direction of the field winding current, the air-gap flux can be flexibly strengthened or weakened, thereby regulating the torque output.

Figure 15 shows the output torque characteristics under different field winding currents with a constant armature current of 15 A and no-load cogging torque. To quantitatively evaluate the torque performance, a torque ripple factor T_{ripple} is introduced, defined as:

$$T_{ripple} = \frac{T_{\max} - T_{\min}}{T_{avg}} \times 100\% \tag{12}$$

where $T_{\max}$, $T_{\min}$, and T_{avg} are the maximum, minimum, and average torque values, respectively. T_{ripple} quantifies the quality of the torque waveform. A comparison was made among flux-weakening current, flux-strengthening current, and PM-only excitation. The corresponding average torque values are 8.17 Nm, 9.19 Nm, and 8.43 Nm, with torque ripple values of 5.4%, 6.3%, and 5.4%, respectively. When the flux-strengthening current is applied, the torque increases by 9.5% compared to the PM-only case, without a significant increase in torque ripple. This indicates that the flux-strengthening operation can effectively enhance the output torque capability. The peak-to-peak cogging torque is 10.3 mNm. Compared to the rated torque output of 8.17 Nm, this value constitutes only 0.13%, demonstrating an exceptionally low level of inherent torque pulsation. This desirable characteristic is primarily attributed to the 12-slot/10-pole fractional-slot concentrated winding configuration, which effectively minimizes cogging torque and contributes to the smooth operation of the motor. Furthermore, the low torque ripple is a direct result of the sinusoidal air-gap flux density and the correspondingly low harmonic distortion in the back EMF.

Figure 16 shows the relationship between the average torque and the current angle at the rated armature current of 15 A. Due to the reverse-salient characteristic, the maximum torque is achieved at a current angle of approximately 12°. This demonstrates that the motor can operate in the flux-strengthening region with $i_d > 0$, thereby fully utilizing the reluctance torque and validating the superior output torque performance of the reverse-salient characteristic.

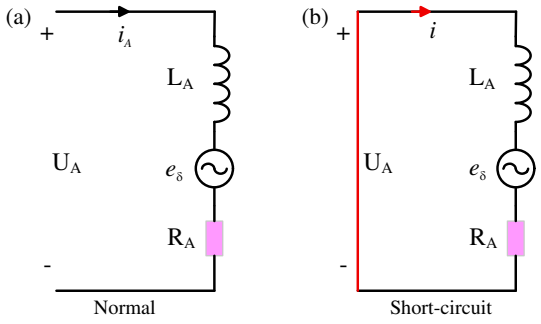

FIGURE 17. Equivalent circuit.

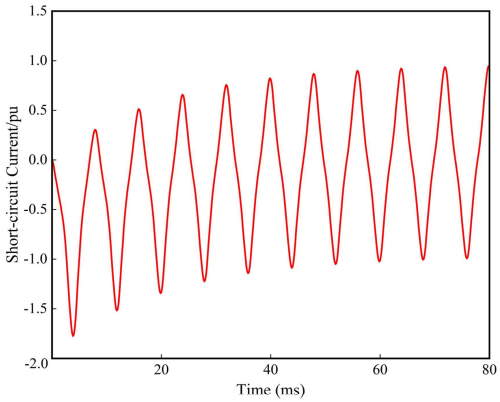

FIGURE 18. Waveform of short-circuit current.

4.6. Short-Circuit Current Characteristics

Winding short-circuit fault is one of the most common fault types in electric motors. Taking phase A as an example, the short-circuit current under a single-phase short-circuit condition is analyzed. Figure 17 shows the equivalent circuits for a phase winding under normal operation and under a terminal short-circuit condition. When a terminal short-circuit occurs, it is assumed that the phase A resistance remains unchanged, and the influence of mutual inductance is neglected. The terminal voltage becomes zero, leading to the fault-state voltage equation given in Equation (13):

$$0 = L_a \frac{di_s}{dt} + e_\delta + R_a i_s \tag{13}$$

where L_a is the winding inductance, i_s the short-circuit current, e_δ the back EMF, and R_a the winding resistance. E_0 is the no-load back EMF. The steady-state short-circuit current derived from Equation (13) is given by Equation (14):

$$i_s = \frac{E_0}{\sqrt{(\omega L_a)^2 + R_a^2}} \tag{14}$$

Figure 18 shows the short-circuit current waveform during a phase A short-circuit fault. The steady-state short-circuit current is only 1.16 times of the rated current, demonstrating the motor's strong short-circuit current suppression capability and validating its high fault-tolerant performance.

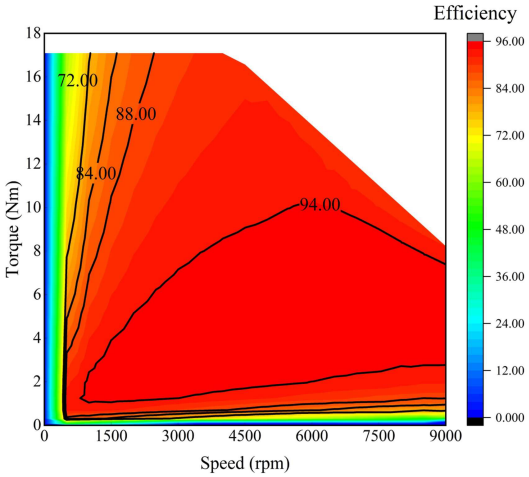

FIGURE 19. Map of efficiency.

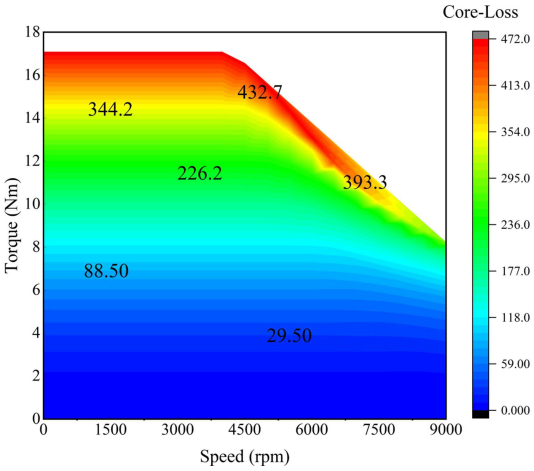

FIGURE 20. Map of loss.

4.7. Efficiency, Losses, and Power Factor

High efficiency is a crucial performance indicator for electric motors. Figure 19 shows the efficiency map of the FT-HE-RSPM at a rated current of 15 A and a DC bus voltage of 125 V. It can be observed that the maximum efficiency of the FT-HE-RSPM reaches 92% under rated conditions. As the speed increases, the peak efficiency reaches approximately 94% around 4500 r/min. With a further increase in speed, the efficiency can achieve 96%. Figure 20 presents the power loss map of the motor. The maximum power loss is 372.5 W under rated operating conditions. In the high-speed region, at 9000 r/min, the maximum loss is 187 W. This reduction in loss and improvement in efficiency are attributed to significant flux leakage in the high-speed flux-weakening field of the FT-HE-RSPM. The power factor is another key performance metric, which reflects the effective utilization of electrical energy during operation. Figure 21 presents the power-factor map of the motor. Under rated conditions, the motor's power factor is approximately 0.78. As the speed increases, the power factor gradually rises to 0.98. This improvement is a result of the reverse-salient characteristic achieved in the proposed motor. The increased d-axis inductance effectively addresses the issue of low power factor in traditional motors during high-speed operation.

The analysis of efficiency map data reveals that the motor achieves 92% efficiency under rated conditions and maintains high efficiency across low-speed, rated, and high-speed operating regions. However, analysis of the power factor shows a low value of approximately 0.78 at the rated condition (1500 r/min, 8.5 Nm), which improves significantly as the speed increases. This initial low power factor is because, at low speeds, the motor operates with a significant positive d-axis current ($i_d > 0$) to utilize its reverse-salient characteristic for generating positive reluctance torque, thereby boosting the output torque. The flux-strengthening current component i_d increases the total apparent power of the motor, resulting in a lower power factor than PMSM. Furthermore, the reverse-salient characteristic underpins the motor's excellent flux-weakening capability. At high speeds during flux-weakening operation, a larger L_d means that the same negative d-axis current generates a greater demagnetizing voltage. This allows the motor to achieve high-speed operation with a smaller current penalty, consequently extending the speed range and enabling a high power factor.

4.8. Mechanical Strength Analysis

To verify the mechanical integrity of the rotor structure, particularly the magnetic bridges, under all operational conditions, a stress analysis was performed using finite element analysis. The simulation was conducted at both the rated speed of 1500 r/min and the high speed of 9000 r/min. The results, shown in the Figure 22, indicate that the equivalent stress is 26 MPa at 1500 r/min and 82 MPa at 9000 r/min. The maximum stress at high speed is located at the inner diameter of the rotor core and the connection points of magnetic bridges, as expected. Crucially, both values are well below the yield strength of the core material DW310_35 (typically $>$ 310 MPa). This provides a safety factor of over 3.78 even at the high speed, conclusively confirming the structural integrity and safety of the rotor, including magnetic bridges, under all specified operational conditions.

5. FAULT-TOLERANT OPERATION ANALYSIS

5.1. Single-Phase Open-Circuit Fault-Tolerant Control Strategy

Under healthy operating conditions, all phases are energized. The six-phase winding currents are given by Equation (15):

$$\begin{aligned} i_a &= I_m \sin(\omega_e t) \\ i_b &= I_m \sin(\omega_e t - 60^\circ) \\ i_c &= I_m \sin(\omega_e t - 120^\circ) \\ i_d &= I_m \sin(\omega_e t - 180^\circ) \\ i_e &= I_m \sin(\omega_e t - 240^\circ) \\ i_f &= I_m \sin(\omega_e t - 300^\circ) \end{aligned} \tag{15}$$

where I_m is the amplitude of the phase current, and ω_e is the electrical angular frequency. It can be seen that the armature windings in the six-phase motor can be considered as two sets of three-phase windings with a 180° phase shift. Therefore, when a single-phase open-circuit fault occurs, the analysis method for a three-phase motor with a single-phase open-circuit fault can

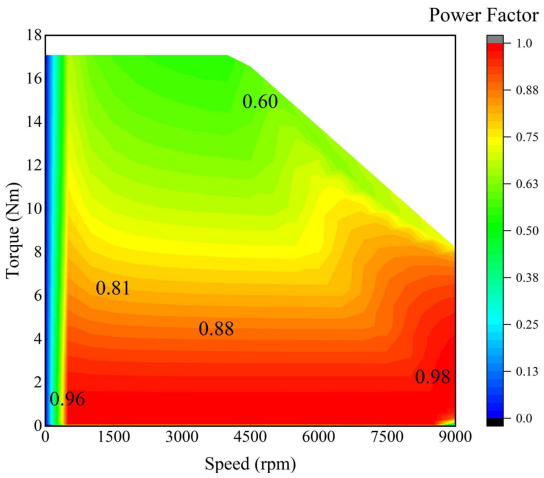

FIGURE 21. Map of power-factor.

be applied. If phase A is open-circuited, one method to maintain the rotating magnetomotive force (MMF) is to control the current amplitude and phase angle in phases C and E. However, the currents in the remaining five phases remain highly unbalanced under this scheme. The second set of stator windings can be utilized to improve the current distribution.

For a six-phase motor with an open-circuit fault in phase A, to achieve continued fault-tolerant operation by producing a circular rotating MMF, the currents in the remaining phases must be reconfigured [27, 28]. The constraints for generating a circular rotating MMF are given by Equations (16), (17):

$$\begin{aligned} &\cos(60^\circ)\, i'_b + \cos(120^\circ)\, i'_c + \cos(180^\circ)\, i'_d \\ &+ \cos(240^\circ)\, i'_e + \cos(300^\circ)\, i'_f = 3I_m \cos\theta \end{aligned} \tag{16}$$

$$\begin{aligned} &\sin(60^\circ)\, i'_b + \sin(120^\circ)\, i'_c + \sin(180^\circ)\, i'_d \\ &+ \sin(240^\circ) i'_e + \sin(300^\circ) i'_f = 3I_m \sin\theta \end{aligned} \tag{17}$$

where $\theta = \omega_e t$ is the phase angle of the current in healthy operation; i'_b, i'_c, i'_d, i'_e and i'_f are the modified armature currents of the other five phases under fault-tolerant operation. From a phasor perspective, a current phasor can be represented as the sum of two orthogonal components. Thus, the current for phase n is assumed to be decomposed as:

$$I_n = ix_n - jy_n = x_n \cos\theta + y_n \sin\theta \tag{18}$$

By separating the cosine and sine components, normalizing with respect to I_m and substituting into the constraints (16) and (17), the following four equations are derived:

$$\begin{aligned} 0.5x_2 - 0.5x_3 - 1x_4 - 0.5x_5 + 0.5x_6 &= 3 \\ 0.5y_2 - 0.5y_3 - 1y_4 - 0.5y_5 + 0.5y_6 &= 0 \\ \frac{\sqrt{3}}{2}y_2 + \frac{\sqrt{3}}{2}y_3 + 0y_4 - \frac{\sqrt{3}}{2}y_5 - \frac{\sqrt{3}}{2}y_6 &= 3 \\ \frac{\sqrt{3}}{2}x_2 + \frac{\sqrt{3}}{2}x_3 + 0x_4 - \frac{\sqrt{3}}{2}x_5 - \frac{\sqrt{3}}{2}x_6 &= 0 \end{aligned} \tag{19}$$

The goal is to find the current I_n for each phase. To minimize stator copper loss, the current magnitude in each winding should be equal. This introduces an additional constraint for

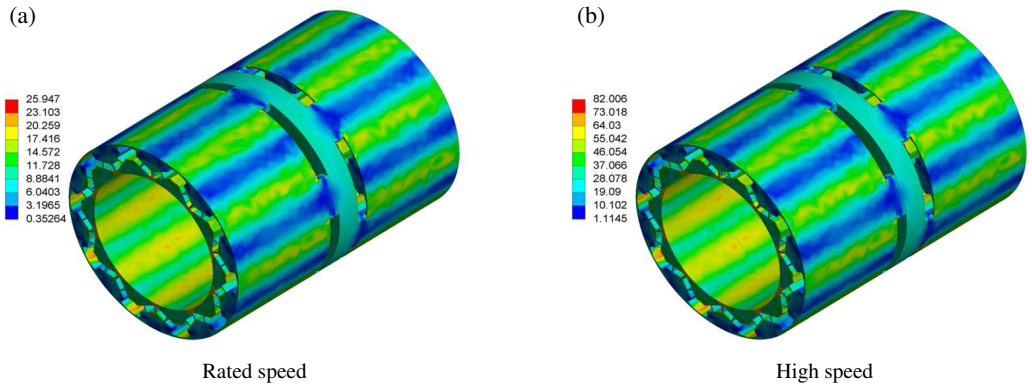

FIGURE 22. Equivalent stress.

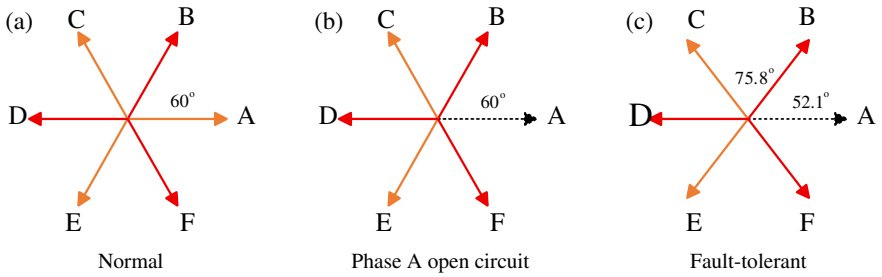

FIGURE 23. Vector diagram of currents.

the optimization:

$$x_{n-1}^2 + y_{n-1}^2 = x_n^2 + y_n^2 \tag{20}$$

Since the number of unknowns exceeds the number of equations, the system has multiple solutions. One set of optimized compensating currents that satisfies the constraints is given by:

$$\begin{aligned} i_b &= I_m \sin(\theta - 52.1^\circ) \\ i_c &= I_m \sin(\theta - 127.9^\circ) \\ i_d &= I_m \sin(\theta + 180^\circ) \\ i_e &= I_m \sin(\theta + 127.9^\circ) \\ i_f &= I_m \sin(\theta + 52.1^\circ) \end{aligned} \tag{21}$$

It is worth noting that the fundamental principle of maintaining a constant rotating MMF, as employed here for the single-phase open-circuit fault, is also applicable to the analysis of other open-circuit fault types (e.g., multi-phase open-circuit). The method for solving the reconfigured currents remains analogous to that described in this section, though the specific solutions differ, and their optimal selection requires separate, detailed investigation.

5.2. Fault-Tolerant Operation Analysis

Therefore, when an open-circuit fault occurs in phase A, the currents in the remaining phases must be reconfigured to maintain the principle of a constant rotating magnetomotive force (MMF). Figure 23 shows the phase current space vectors for both normal operation and post-fault condition with reconfigured currents. Figure 24 compares the output torque under three

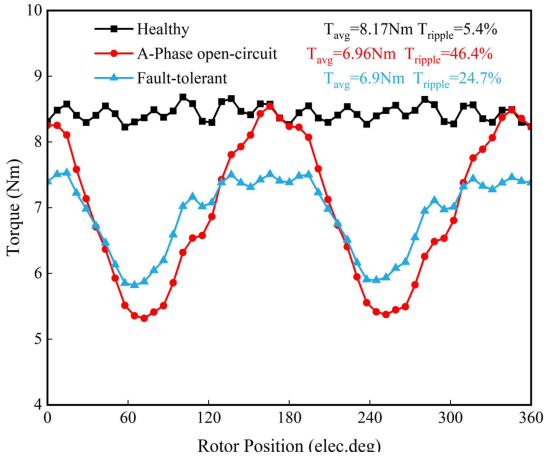

FIGURE 24. Comparison of output torque under different operating conditions.

operating conditions. Under normal operation, the torque is 8.17 Nm with a torque ripple of 5.4%. When an open-circuit fault occurs in phase A, the output torque under the faulty operation state is 6.96 Nm, and the torque ripple increases significantly to 46.4%. This demonstrates the severe detrimental impact a winding open-circuit fault can have on vehicle operation. With the reconfigured currents, the output torque under fault-tolerant operation is 6.90 Nm, and the torque ripple is reduced to 24.7%. Compared to the faulty operation state, the torque ripple in fault-tolerant operation is reduced by 46.4%, validating the motor's excellent fault-tolerant capability for open-circuit operation.

6. CONCLUSION

To address the limitations of conventional permanent magnet synchronous motors (PMSMs) in electric vehicle applications, such as a narrow speed regulation range, weak fault-tolerant capability, and limited torque output, this paper proposes a six-phase 12-slot/10-pole fault-tolerant hybrid-excited reverse-salient permanent magnet motor (FT-HE-RSPM). A rational design of the magnetic bridge and rotor creates an axial magnetic circuit, enabling the regulation of the air-gap flux by controlling the field winding current.

First, the magnetic circuit principle and hybrid excitation regulation mechanism of the proposed motor are analyzed through mathematical derivations.

Second, the electromagnetic characteristics are investigated via finite element analysis (FEA). Regarding flux regulation, the field winding current enables a wide-range control of the flux linkage, with a regulation factor reaching 10.6%. In terms of torque output, benefiting from its excellent flux-strengthening characteristics, the torque is increased by 9.5% with a field winding current $I_f = 20\,\text{A}$. Combined with its reverse-salient characteristic, the motor not only meets the flux-strengthening torque demand under low-speed and high-load conditions but also achieves flux-weakening speed expansion under high-speed and light-load conditions. Regarding efficiency and power factor, the efficiency is 92% under rated conditions and reaches 96% in the high-speed region ($> 4500\,\text{r/min}$). The power factor improves from 0.78 at rated speed to 0.98 at high speed, effectively mitigating the issue of low power factor in conventional motors during high-speed operation.

Finally, targeting the common single-phase open-circuit fault in EVs, the current phases for fault-tolerant operation are reconfigured based on the principle of constant magnetomotive force (MMF). The results show that with this strategy, the motor maintains an output torque of 6.90 Nm while significantly reducing the torque ripple to 24.7%. This validates that the proposed fault-tolerant strategy effectively suppresses the impact of faults on operational stability, ensuring the EV's short-term safe operation capability under fault conditions.

ACKNOWLEDGEMENT

This work was supported in part by the National Natural Science Foundation of China (Grant No. 52067008), in part by the Youth Project of the Natural Science Foundation of Jiangxi Province (20242BAB20219), in part by the Jiangxi Province Early Career Youth Science and Technology Talent Training Project (20244BCE52182) and in part by the Jiangxi Provincial Key Laboratory of Multidimensional Intelligent Perception and Control (No. 2024SSY03161).

REFERENCES

[1] Gallegos, J., P. Arévalo, C. Montaleza, and F. Jurado, "Sustainable electrification-advances and challenges in electrical-distribution networks: A review," *Sustainability*, Vol. 16, No. 2, 698, 2024.

[2] Zhang, X., F. Gao, X. Gong, Z. Wang, and Y. Liu, "Comparison of climate change impact between power system of electric vehicles and internal combustion engine vehicles," in *Advances in Energy and Environmental Materials*, 739–747, Singapore, 2018.

[3] Zheng, J., W. Zhao, J. Ji, and C. H. T. Lee, "Quantitative analysis on maximum efficiency point and specific high-efficiency region of permanent-magnet machines," *IEEE Transactions on Industrial Electronics*, Vol. 69, No. 2, 1333–1345, Feb. 2022.

[4] Hlioui, S., M. Gabsi, H. B. Ahmed, G. Barakat, Y. Amara, F. Chabour, and J. J. H. Paulides, "Hybrid excited synchronous machines," *IEEE Transactions on Magnetics*, Vol. 58, No. 2, 1–10, Feb. 2022.

[5] Du, L., X. Liu, J. Fu, J. Liang, and C. Huang, "Design and optimization of reverse salient permanent magnet synchronous motor based on controllable leakage flux," *CES Transactions on Electrical Machines and Systems*, Vol. 5, No. 2, 163–173, Jun. 2021.

[6] Kosaka, T., M. Sridharbabu, M. Yamamoto, and N. Matsui, "Design studies on hybrid excitation motor for main spindle drive in machine tools," *IEEE Transactions on Industrial Electronics*, Vol. 57, No. 11, 3807–3813, Nov. 2010.

[7] Contò, C. and N. Bianchi, "A hybrid-excitation synchronous motor with a change in polarity," *Machines*, Vol. 10, No. 10, 869, 2022.

[8] Mudhigollam, U. K., U. Choudhury, and K. Hatua, "A new rotor excitation topology for hybrid excitation machine," in *2016 IEEE International Conference on Power Electronics, Drives and Energy Systems (PEDES)*, 1–6, Trivandrum, India, 2016.

[9] Liu, Y., Z. Zhang, and X. Zhang, "Design and optimization of hybrid excitation synchronous machines with magnetic shunting rotor for electric vehicle traction applications," *IEEE Transactions on Industry Applications*, Vol. 53, No. 6, 5252–5261, Nov.-Dec. 2017.

[10] Wang, H., Y. Xue, J. Du, and H. Li, "Design and evaluation of modular stator hybrid-excitation switched reluctance motor for torque performance improvement," *IEEE Transactions on Industrial Electronics*, Vol. 71, No. 10, 12 814–12 823, Oct. 2024.

[11] Xu, L., X. Zhu, T. Jiang, and S. Niu, "Design and optimization of a partitioned stator hybrid excited machine with inset PM from perspective of airgap field harmonics," *IEEE Transactions on Energy Conversion*, Vol. 38, No. 4, 2871–2883, Dec. 2023.

[12] Meng, Y., X. Yang, H. Chen, S. Fang, and Q. Xu, "Design and analysis of a new hybrid-excited flux switching machine with dual-set of PMs," *IEEE Transactions on Industrial Electronics*, 1–12, 2025.

[13] Yao, F., Q. An, X. Gao, L. Sun, and T. A. Lipo, "Principle of operation and performance of a synchronous machine employing a new harmonic excitation scheme," *IEEE Transactions on Industry Applications*, Vol. 51, No. 5, 3890–3898, Sep.-Oct. 2015.

[14] Dutta, R. and M. F. Rahman, "Design and analysis of an interior permanent magnet (IPM) machine with very wide constant power operation range," *IEEE Transactions on Energy Conversion*, Vol. 23, No. 1, 25–33, Mar. 2008.

[15] Zhao, X., B. Kou, and C. Huang, "A reverse-salient permanent magnet synchronous motor and its *dq*-axis current distribution laws," *IEEE Transactions on Industrial Electronics*, Vol. 70, No. 4, 3337–3347, Apr. 2023.

[16] Zhao, X., B. Kou, L. Zhang, and H. Zhang, "Design and analysis of permanent magnets in a negative-salient permanent magnet synchronous motor," *IEEE Access*, Vol. 8, 182 249–182 259, 2020.

[17] Zhao, X., B. Kou, C. Huang, and L. Zhang, "A reverse-salient permanent magnet synchronous motor for electric vehicles considering operating conditions," *IEEE Transactions on Energy Conversion*, Vol. 38, No. 1, 262–272, Mar. 2023.

[18] Zhu, X., J. Huang, L. Quan, Z. Xiang, and B. Shi, "Comprehensive sensitivity analysis and multiobjective optimization research of permanent magnet flux-intensifying motors," *IEEE Transactions on Industrial Electronics*, Vol. 66, No. 4, 2613–2627, Apr. 2019.

[19] Zhang, G., W. Hua, M. Cheng, and J. Liao, "Design and comparison of two six-phase hybrid-excited flux-switching machines for EV/HEV applications," *IEEE Transactions on Industrial Electronics*, Vol. 63, No. 1, 481–493, Jan. 2016.

[20] Zhang, L., Y. Fan, R. D. Lorenz, R. Cui, C. Li, and M. Cheng, "Design and analysis of a new five-phase brushless hybrid-excitation fault-tolerant motor for electric vehicles," *IEEE Transactions on Industry Applications*, Vol. 53, No. 4, 3428–3437, Jul.–Aug. 2017.

[21] Xu, W., F. Ying, Y. Yu, G. Yang, and C. H. T. Lee, "Design and analysis of a five phase dual stator hybrid excitation machine with spoke-type permanent magnet rotor," in *2023 26th International Conference on Electrical Machines and Systems (ICEMS)*, 1987–1992, Zhuhai, China, 2023.

[22] Deng, S., L. Zhang, and D. Shen, "Investigation on wide-speed operation of a new five-phase fault-tolerant interior permanent magnet motor from perspective of flux-intensifying effect," *IEEE Transactions on Magnetics*, Vol. 59, No. 11, 1–6, Nov. 2023.

[23] Zhang, L., X. Li, X. Zhu, and C. Zhang, "Design and optimization of a five-phase reverse-salient fault-tolerant permanent magnet motor for electric vehicles," *IEEE Transactions on Industrial Electronics*, Vol. 72, No. 7, 6762–6774, Aug. 2025.

[24] Zhu, S., W. Zhao, J. Ji, G. Liu, and C. H. T. Lee, "Design to reduce modulated vibration in fractional-slot concentrated-windings PM machines considering slot–pole combination," *IEEE Transactions on Transportation Electrification*, Vol. 9, No. 1, 575–585, Mar. 2023.

[25] Wu, L., R. Qu, and D. Li, "Reduction of rotor eddy-current losses for surface PM machines with fractional slot concentrated windings and retaining sleeve," *IEEE Transactions on Magnetics*, Vol. 50, No. 11, 1–4, Nov. 2014.

[26] Zhang, G., W. Hua, M. Cheng, J. Liao, K. Wang, and J. Zhang, "Investigation of an improved hybrid-excitation flux-switching brushless machine for HEV/EV applications," *IEEE Transactions on Industry Applications*, Vol. 51, No. 5, 3791–3799, Sep.-Oct. 2015.

[27] Fu, J.-R. and T. A. Lipo, "Disturbance-free operation of a multiphase current-regulated motor drive with an opened phase," in *Conference Record of the 1993 IEEE Industry Applications Conference Twenty-Eighth IAS Annual Meeting*, Vol. 1, 637–644, Toronto, ON, Canada, 1993.

[28] Rahmatullah, R., N. F. O. Serteller, and V. Topuz, "Modeling and simulation of faulty induction motor in DQ reference frame using MATLAB/SIMULINK with MATLAB/GUIDE for educational purpose," *International Journal of Education and Information Technologies*, Vol. 17, 7–20, 2023.